

Ocean wave directional spectra estimation from an HF ocean radar with a single antenna array: Observation

Yukiharu Hisaki

Department of Physics and Earth Sciences, Faculty of Science, University of the Ryukyus, Okinawa, Japan

Received 16 January 2005; revised 17 June 2005; accepted 11 August 2005; published 4 November 2005.

[1] A method of estimating ocean wave directional spectra using a high-frequency (HF) radar with a single antenna array was applied to actual ocean data. This method incorporates the wave energy balance equation and the continuity equation of wind vectors into the inversion method to solve the integral equation which relates a Doppler spectrum to wave spectra. This method uses dynamic extrapolation to estimate wave spectra at positions where the signal-to-noise (SN) ratio in Doppler spectra is not high. The agreement of wave heights with in situ observation is good. Additionally, there is a correlation between radar-estimated sea surface winds and winds near the HF radar observation area. The method under consideration was found to be able to estimate wave directional spectra in swell conditions.

Citation: Hisaki, Y. (2005), Ocean wave directional spectra estimation from an HF ocean radar with a single antenna array: Observation, *J. Geophys. Res.*, 110, C11004, doi:10.1029/2005JC002881.

1. Introduction

[2] It is important to be able to estimate ocean surface wave spectra for a wide variety of marine applications including uses in physical oceanography, wave forecasting, ship routines and coastal engineering. One promising technology for wave measurement is high-frequency (HF) ocean radar, which radiates HF radio waves to the sea surface and measures ocean surface currents [Barrick *et al.*, 1977; Prandle and Ryder, 1985; Takeoka *et al.*, 1995; Hisaki *et al.*, 2001; Hisaki and Naruke, 2003] and surface waves [Hisaki, 1996, 2002, 2004, 2005] by analyzing the Doppler spectra of backscattered signals.

[3] Ocean wave directional spectra can be estimated from first- and second-order Doppler spectra by inverting the integral equation which relates a given ocean wave spectrum to the Doppler spectrum [Wyatt, 1990; Howell and Walsh, 1993; Hisaki, 1996; Hashimoto and Tokuda, 1999; Hashimoto *et al.*, 2003]. The Doppler spectrum is described by the integral forms of the wave spectrum on the basis of HF radio wave scattering theory from the sea surface [Barrick, 1971; Hisaki, 1999; Hisaki and Tokuda, 2001]. The integral equation is the nonlinear form, as adopted by Hisaki [1996], Hashimoto and Tokuda [1999] and Hashimoto *et al.* [2003], while Wyatt [1990] and Howell and Walsh [1993] adopted the linear inversion. The narrow beam radar system, which is capable of measuring waves at a high resolution, was used in these studies. However, the derivation of wave spectra from the second-order Doppler spectrum is fragile, because the second-order Doppler is close to the noise level and is therefore often contaminated.

In addition, a large area is required to deploy the antenna system. To ameliorate these problems, Hisaki [2005] developed a method of estimating ocean wave spectra with a single radar. To the best of our knowledge, this is the first method that incorporates the wave model into the inversion method to estimate wave spectra from HF ocean radar. The wave energy balance equation and the two-dimensional continuity equation of surface winds are used for the inversion method. Identical twin experiments were conducted: wave spectra were simulated from the wave energy balance equation, and Doppler spectra were calculated from simulated wave spectra. The wave spectra were retrieved from calculated Doppler spectra. It is shown that this method can dynamically extrapolate wave spectra even in an inhomogeneous wave field from identical twin experiments. Ocean wave directional spectra can be estimated even at positions where only first-order Doppler spectra are available by incorporating the wave energy balance equation. Nevertheless, this new method was not applied to actual ocean data by Hisaki [2005]. The purpose of the present study was to apply the method developed by Hisaki [2005] to actual Doppler spectra obtained from HF radar observation, and to compare wave parameters with in situ observations.

[4] The method of estimating wave spectra is briefly reviewed in section 2. Observations and data analysis are described in section 3, and results are presented in section 4. The conclusions and issues for future research are summarized in section 5.

2. Methods

2.1. Formulation

[5] The mathematical details of the inversion method are described by Hisaki [2005], and briefly reviewed here. A

Doppler spectrum $P(\omega_D)$, which shows two sharp peaks at $\omega_D = \pm\omega_B$, is obtained on a polar grid point with origin at the radar position, where ω_D is a radian Doppler frequency $\omega_B = (2gk_0)^{1/2}$ (deep water) is the radian Bragg frequency, k_0 is the radio wave number, and g is the gravitational acceleration. Wave spectra are estimated on the polar grid points. The wave directional spectra $G(\omega, \theta, r, \psi) = G(k_f, l_d, i_r, l_d)$ at radian frequencies ω , wave directions θ and polar coordinates (r, ψ) are estimated for grid points $(\omega(k_f), \theta(l_d), r(i_r), \psi(j_b))$ ($\omega = \omega(k_f) = \omega_{\min} \Delta_\omega^{k_f-1}$, $\theta = \theta(l_d) = -\pi + 2\pi(l_d - 1)/M_d$, $r = r(i_r) = r_{\min} + \Delta_r(i_r - 1)$, $\psi = \psi(j_b) = \psi_{\min} + \Delta_\psi(j_b - 1)$, $k_f = 1, \dots, M_f$, $l_d = 1, \dots, M_d$, $i_r = 1, \dots, N_r$, $j_b = 1, \dots, N_B$) in four-dimensional space ($\omega - \theta - r - \psi$: wave frequency–wave direction–polar plane), where $\omega(k_f)$ is the wave radian frequency for a frequency number k_f , ω_{\min} is the minimum radian frequency, Δ_ω is the frequency increment, $\theta(l_d)$ is the wave direction for a direction number l_d , $r(i_r)$ is the distance between the radar and a grid point for a range (index) number i_r , r_{\min} is the closest distance from the radar, Δ_r is the range resolution, $\psi(j_b)$ is the beam direction for a beam (index) number j_b (hereafter the direction is understood to be the counterclockwise angle with respect to the eastward direction), ψ_{\min} is the rightmost direction, and Δ_ψ is the beam resolution. The number N_r is the number of ranges, N_B is the number of beams, M_f is the number of wave frequencies, and M_d is the number of wave directions. In addition to wave spectra, 10-m sea surface wind speeds $u_w = u_w(i_r, j_b)$ and wind directions $\theta_w = \theta_w(i_r, j_b)$ at the grids (i_r, j_b) are also estimated as explained below.

[6] The assumptions of the present method are the following: First, the perturbation theory of HF radio wave scattering can be applied, and the wave height is not high; the wave field and winds are almost stationary in time; and finally, the winds and wave fields are homogeneous in each radar cell with radial resolution Δr and azimuthal resolution Δ_ψ .

[7] The equations for estimating wave spectra are: (1) the relationship between first-order Doppler spectra and wave spectra, (2) the relationship between second-order Doppler spectra and wave spectra, (3) the wave energy balance equation under the assumption of stationarity, (4) the continuity equation of wind vectors under the assumption of no horizontal divergence, (5) regularization constraints in frequency-direction grids, and (6) regularization constraints in spatial radial grids. These constraints shall be referred to as constraints C1–C6. Constraints C1 and C2 are written as

$$\log \left[\int_0^\infty \sigma_1((2m-3)\omega_D) d\omega_D \right] - \log \left[\int_{-\infty}^\infty \sigma_1(\omega_D) d\omega_D \right] \\ = \log \left[\int_0^\infty P_{c1}((2m-3)\omega_D) d\omega_D \right] \quad (m = 1 \text{ or } 2) \quad (1)$$

$$\log(\sigma_2(\omega_D)) - \log \left[\int_{-\infty}^\infty \sigma_1(\omega_D) d\omega_D \right] = \log(P_{c2}(\omega_D)), \quad (2)$$

respectively, where

$$P_{ci}(\omega_D) = P_i(\omega_D) \left[\int_{-\infty}^{+\infty} P_1(\omega_D) d\omega_D \right]^{-1} \quad (3)$$

are the first- ($i = 1$) and second-order ($i = 2$) calibrated Doppler spectral densities, and $P_1(\omega_D)$ and $P_2(\omega_D)$ are the first- and second-order Doppler spectral densities: ($P(\omega_D) = P_1(\omega_D) + P_2(\omega_D)$). The calibration factor in equation (3) is estimated by integrating the Doppler spectrum $P(\omega_D)$ with respect to ω_D over the finite Doppler frequency band, which is determined by identifying local minima around the two first-order scattering peaks. The first-order radar cross section $\sigma_1(\omega_D)$ in equation (1) is written in terms of a wave directional spectrum $G(\omega, \theta)$ as in equation (1) of *Lipa and Barrick* [1986] and in equation (13) of *Hisaki* [1996]. The integral of $\sigma_1((2m-3)\omega_D)$ with respect to ω_D in the present equation (1) is proportional to $G(\omega, \theta)$ at $(\omega, \theta) = (\omega_B, \psi(j_b) + (m-1)\pi)$. The second-order radar cross-section $\sigma_2(\omega_D)$ in equation (2) is written by equation (3) of *Lipa and Barrick* [1986] and by equation (18) of *Hisaki* [1996], which can be expressed in terms of $G(\omega, \theta)$.

[8] Constraint C3 is expressed as

$$\mathbf{C}_g \cdot \nabla G(\omega, \theta) - S_t = 0, \quad (4)$$

where \mathbf{C}_g is a group velocity vector, S_t is the source function, and ∇ denotes horizontal gradient. The source function S_t is the sum of the wind input source function, the nonlinear transfer source function and the dissipation source function. The effect of bottom friction is ignored. The parameterization of the source functions are the same as those presented in WAM cycle 3 [*WAMDI group*, 1988]. The wind input source function is expressed not only by the wave spectrum $G(\omega, \theta)$ but also by the surface wind vector $\mathbf{u}_w = (u_w \cos \theta_w, u_w \sin \theta_w)$.

[9] Constraint C4 is expressed as

$$\nabla \cdot \mathbf{u}_w = 0. \quad (5)$$

Equation (5) is expressed by the polar coordinate with origin at the radar position.

[10] Constraint C5 is expressed as

$$\log(G(k_f + 1, l_d)) + \log(G(k_f - 1, l_d)) \\ + \log(G(k_f, l_d - 1)) + \log(G(k_f, l_d + 1)) \\ - 4 \log(G(k_f, l_d)) = 0 \quad \text{for } 1 < k_f < M_f, \\ \text{or} \\ \log(G(k_f, l_d - 1)) + \log(G(k_f, l_d + 1)) \\ - 2 \log(G(k_f, l_d)) = 0 \quad \text{for } k_f = 1, M_f, \quad (6)$$

where $G(k_f, l_d) = G(k_f, l_d, i_r, j_b)$ is the wave directional spectrum for frequency number k_f and direction number l_d .

[11] Constraint C6 is

$$\mathbf{C}_g \cdot \nabla G(\omega, \theta) = 0, \quad (7)$$

which is introduced not only to avoid large spatial variations of wave spectral values in the polar plane, but also to reduce the underestimation of wave height when the dominant wave propagates perpendicular to the beam direction [*Wyatt*, 2002]. In practice, the addition of this constraint does not significantly increase computation time, because equation (7) is computed simultaneously with constraint C3 (equation (4)).

[12] The unknowns to be estimated are wave spectral values and wind vectors. The number of the unknowns is

$N_u = N_s + 2N_g$, where $N_g = N_r N_B$ is the number of radial grids, and $N_s = M_f M_d N_g$ is the total number of spectral values. The total number of constraints is $N_t = 3N_s + 2N_g + K_{DT}$, where K_{DT} is the total number of second-order Doppler spectral values for wave estimation. The equations are normalized by the Bragg parameter $2k_0$ and ω_B as presented by *Lipa and Barrick* [1986]. These equations are discretized in terms of wave spectral values in four-dimensional space ($\omega - \theta - r - \phi$: wave frequency-wave direction-polar plane), and wind vectors on the polar grids.

[13] Thus, we seek the N_u -dimensional vector \mathbf{x} to minimize the objective function defined as a sum of the weighted squared differences of constraints (C1)–(C6) (equations (1), (2), (4), (5), (6) and (7), respectively), or

$$U(\mathbf{x}) = \frac{1}{2} \sum_{K=1}^{N_t} [\lambda_{wM} F_K(\mathbf{x})]^2, \quad (8)$$

where the N_u -dimensional vector $\mathbf{x} = (x_L)$ ($L = 1, \dots, N_u$) denotes spectral values, wind speeds and directions, and F_K corresponds to constraints (C1)–(C6). The component x_L denotes $\log(G(k_f, l_d, i_r, j_b))$ for $L \leq N_s$, $\log(u_w(i_r, j_b))$ for $N_s < L \leq N_g + N_s$, and $\theta_w(i_r, j_b)$ for $N_g + N_s < L \leq N_u$. The parameter λ_{wM} ($M = 1, \dots, 6$) is the weight for constraints (C1)–(C6).

2.2. Algorithm

[14] The process used to determine the value of \mathbf{x} consists of three steps. The first step is to estimate a wave spectrum in a parametric form, the wave spectra being independent of radial grids. The initial spectrum is actually the result of fitting the equations for the first- and second-order Doppler spectra with a range of model wave spectral parameters, which are assumed to apply over the total scattering region. The wave spectrum is estimated from constraints (C1) and (C2) (equations (1) and (2)), and the parameters used to describe the initial spectrum are estimated by the Monte Carlo method. These parameters are randomly generated for pre-decided parameter ranges, seeking parameters which will minimize the sum of the weighted squared differences of constraints (C1) and (C2). Wind direction is also estimated in the first step, with the initial wind direction estimated from the ratio of first-order scattering as in the method described by *Hisaki* [2002].

[15] The wave spectra are also independent of radial grids in the second step, and the number of spectral values is $M_f M_d$, where M_f is the number of wave frequencies and M_d is the number of wave directions. The $M_f M_d$ spectral values are estimated in the second step from constraints (C1), (C2) and (C5) (equations (1), (2), and (6)), minimizing the sum of the weighted squared differences of these constraints by a nonlinear minimization method such as the Levenberg-Marquardt Method. The initial wind speed is estimated from an initial frequency spectral value at a high frequency in the second step. The wave spectra are estimated by integrating in advance the energy balance equation ($\partial G/\partial t = S_t$) with respect to time t until stationary conditions for various wind speeds. The wind speed is inferred from an initial frequency spectral value at a high frequency by comparing the spectra calculated from the energy balance equation. The initial guesses of wave spectra and wind vectors are determined by the second step.

[16] The vector \mathbf{x} to minimize $U(\mathbf{x})$ (equation (8)) is estimated in the third step using the iterative algorithm [Hisaki, 2005]. If the number of unknowns is too large (for example, $N_u = 6080$ in section 3.1), nonlinear minimization methods such as the Levenberg-Marquardt Method cannot be used because of the computer memory storage problem. In the present study, we use the steepest descent method or a modified form of the steepest descent method: The update vector is obtained by multiplying the gradient vector of $U(\mathbf{x})$ (equation (8)) by a positive definite diagonal matrix from the left [Hisaki, 2005]. In this case, the update vector of the iterative algorithm has the same form as equations (49)–(52) and (55)–(58) of *Hisaki* [1996], and the computer memory storage problem can thus be avoided. The algorithm in the third step guarantees that the objective function $U(\mathbf{x})$ can be reduced in each iteration. It is rare that an algorithm with an unusually large number of unknowns ($N_u = 6080$) converges on the solution minimizing the objective function $U(\mathbf{x})$ completely in a short period of computation time. There were no cases that the algorithm converged completely. The algorithm is terminated by the number of iterations, and the maximum iteration number is 105. This maximum iteration number cannot be so large that a long computation time is required. The number 105 is likely to be valid based on the results presented in section 4. The initial wave spectra in the first step are different from final estimated spectra, and the algorithm is robust to the initial guess in the first step based on the simulation results [Hisaki, 2005]. However, the iteration is terminated by the limited number of iterations, and the estimated solution is dependent on the initial guess in the second step. The dependency of estimated wave heights on the initial guess in the second step is discussed in section 4.4.

[17] The wind speeds and directions are also updated in the third step, however, modifications to them are small. The wind speeds and directions are determined primarily in the second and first steps, respectively.

3. Observations

3.1. HF Ocean Radar

[18] Observation of surface currents and waves was conducted from 21 August to 10 September 1995 east of Okinawa Island using the HF ocean radars of the Okinawa Radio Observatory, Communications Research Laboratory (Okinawa Subtropical Environment Remote-Sensing Center, National Institute of Information and Communications Technology). Figure 1 shows a map of the observation area. Observation was conducted as described by *Hisaki and Naruke* [2003]. Radars were located at sites A ($26^\circ 04' 48''\text{N}$, $127^\circ 41' 23''\text{E}$) and B ($26^\circ 16' 55''\text{N}$, $127^\circ 48' 26''\text{E}$) shown in Figure 1, but only the radar at site A was used for the present analysis. The radio frequency was 24.5 MHz, the radar wavelength was $2\pi/k_0 = 12.2$ m, and the Bragg frequency was $f_B = \omega_B/(2\pi) = (2gk_0)^{1/2}/(2\pi)$ is 0.506 Hz, where g is gravitational acceleration.

[19] The range resolution of the radar was 1.5 km. The radar was of the beam-forming type, with the beam-forming electronically controlled by a phase shifter in real time. The beam step was 7.5° , and the time step was 10 min. The total beam number was 12, and Doppler spectra were obtained every 2 hours; wave spectra were also estimated at 2-hour

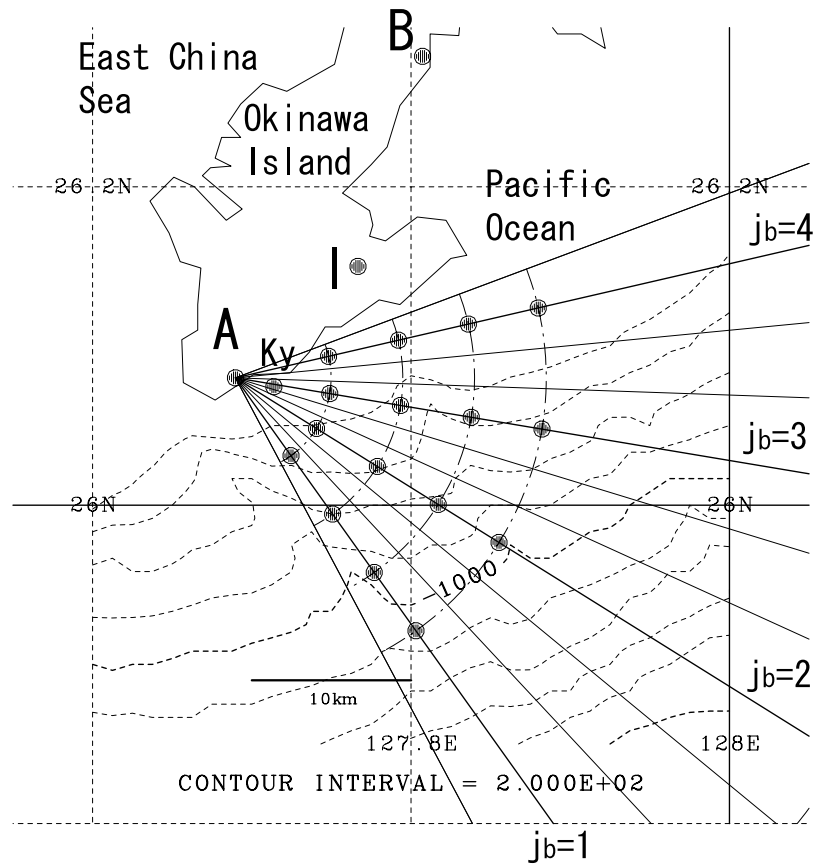


Figure 1. HF radar observation area. Black points indicate radial grids used to estimate wave spectra. The beam index number j_b is indicated. A, B: radar positions; Ky: Japan Meteorological Agency (JMA) wave observation point; I: JMA wind observation point.

intervals. The radar system is described in detail by *Hisaki et al.* [2001].

3.2. Other Data

[20] Significant wave heights (H_s) and wave periods (T_s) at the location Kyan (Ky in Figure 1, $26^\circ 4'N$, $127^\circ 43'E$) were observed by the Japan Meteorological Agency (JMA) at 1-hour intervals. The acoustic wave sensor at a water depth of 51 m and located 1370 m off the coast measured surface waves at 0.25-s intervals. The significant wave heights and periods were estimated by the zero-up-cross method [e.g., *Goda*, 2000] based on 20 min of observation (4800 samples) of surface displacements. The wave analysis data at $26^\circ N$, $128^\circ E$ at 24-hour intervals (every 9 Japan Standard Time) was supplied by the *Japan Meteorological Agency* [1996] and predicted by them using the numerical wave model presented by *Uji* [1984] and adopted for wave prediction by the JMA in 1995. Surface wind data taken at 10-min intervals at the location Itokazu (I in Figure 1, $26^\circ 09'N$, $127^\circ 46'E$, elevation: 186 m) were also supplied by the JMA. The resolutions of wind speeds and directions are 1 m/s and 22.5° , respectively.

3.3. Doppler Spectra Processing and Parameters

[21] The Doppler spectra were averaged in order to reduce the computation time and the computer memory

requirements, even though the spatial resolution of averaged Doppler spectra is coarser than that of the original Doppler spectra. Three neighboring Doppler spectra were averaged in the direction of the radar beam, and the three neighboring Doppler spectra were averaged in the radar range direction. Thus nine Doppler spectra were averaged; the center grid of the nine Doppler spectra is indicated in Figure 1. The number of radial grid points in Figure 1 is one ninth of that of the radial grid points for the original Doppler spectra. The Doppler shift of the first-order peaks from the Bragg frequency by surface currents in the Doppler spectrum was corrected before averaging Doppler spectra. The range and beam resolutions of averaged Doppler spectra are 3 times larger than those of original spectra owing to averaging. The parameters of the spatial resolution are given by $\Delta_r = 4.5$ km, $\Delta_\psi = 22.5^\circ$, and the number of beams by $N_B = 4$. Other radar parameters are $r_{\min} = 6$ km, $\psi_{\min} = -54.5^\circ$, number of ranges $N_r = 4$, and largest range $r_{\max} = r_{\min} + (N_r - 1)\Delta_r = 19.5$ km. The azimuthal resolutions in kilometers are $r_{\min} \Delta_\psi = 2.36$ km at the range r_{\min} , and $r_{\max} \Delta_\psi = 7.66$ km at the range r_{\max} . The boresight direction was $\psi_a = -20.75^\circ$.

[22] The parameters of the wave spectrum are the frequency increment $\Delta_\omega = 1.15$, the number of wave frequencies $M_f = 21$, the number of wave directions $M_d = 18$, minimum frequency $f_{\min} = \omega_{\min}/(2\pi) = 0.0497$ Hz, and maximum frequency $f_{\max} = \omega_{\max}/(2\pi) = 0.813$ Hz. The total

number of unknowns (spectral values, wind speeds and directions) is $N_u = M_f M_d N_r N_B + N_r N_B = 6080$.

[23] Doppler spectra are often contaminated by noise, so it is necessary to extract Doppler frequency ranges of second-order Doppler spectra from Doppler spectra. Doppler frequency ranges of second-order Doppler spectra are extracted by sorting the Doppler spectral values from the smallest to the largest; the noise level d_n is then calculated by averaging the lowest half of the Doppler spectral values. It is assumed that the signal levels in lowest half of the Doppler spectral values are much smaller than both the noise level and second-order Doppler spectral values for wave estimation. Doppler frequency ranges of first-order Doppler spectra $[\omega_{Dl}(m), \omega_{Du}(m)]$ ($m = 1, 2$) are determined, where $m = 1$ denotes negative Doppler frequency, and $m = 2$ denotes positive Doppler frequency. The Doppler frequency bands $[\omega_{Dl}(m), \omega_{Du}(m)]$ ($m = 1, 2$) are determined by identifying local minima around the two first-order peaks. The second-order Doppler peaks are also identified from the four sidebands that surround the first-order Doppler peaks. The second-order Doppler peaks of the four sidebands are sought in Doppler frequency ranges $-1.6\omega_B < \omega_D < \omega_{Dl}(1)$, $\omega_{Du}(1) < \omega_D < -0.5\omega_B$, $0.5\omega_B < \omega_D < \omega_{Dl}(2)$, and $\omega_{Du}(2) < \omega_D < 1.6\omega_B$. If the second-order Doppler peak level in a given Doppler frequency range is larger than the threshold, the second-order Doppler peak is identified. This criterion is $10\log_{10}(S_p) \geq 10\log_{10} d_n + 10\log_{10} 3$, where S_p is the second-order Doppler peak level. The second-order Doppler peak level is larger than the noise level by more than 3 dB. If the second-order Doppler peak does not meet the threshold, the sideband is not used for wave estimation.

[24] The number of sidebands used for wave estimation (from zero to four) is dependent on the signal-to-noise (SN) ratio of the Doppler spectrum. In cases in which no sideband is used for wave estimation, the wave spectrum at the position is interpolated or extrapolated from the constraints C3 (equation (4)) and C6 (equation (7)). Because the spectra at different positions are related by the propagation term ($C_g \cdot \nabla G(\omega, \theta)$) in equations (4) and (7), the spectrum at a radial point where the second-order scattering is unavailable, is inferred from equations (4) and (7). If a second-order Doppler peak is identified, the Doppler frequency range of the second-order Doppler spectrum is identified in the surrounding Doppler frequency range. The identified second-order Doppler spectral level is also larger than the noise level by more than 3 dB.

[25] Figure 2 shows examples of averaged Doppler spectra for each (i_r, j_b) ($i_r = 1, \dots, N_r, j_b = 1, \dots, N_B$), where i_r is the range (index) number, and j_b is the beam (index) number. The validity of the identification of the Doppler frequency range of the second-order Doppler spectrum is confirmed from the figures of Doppler spectra shown in Figure 2. The second-order Doppler frequency ranges are also indicated in Figure 2. These second-order ranges were extracted from two or three sidebands for $j_b = 1$ (Figure 2a), from two sidebands for $j_b = 2$ and 3, (Figures 2b and 2c) and from one or two sidebands for $j_b = 4$ (Figure 2d). The SN ratio in the Doppler spectra for beam $j_b = 4$ is the poorest of all obtained examples. The HF ocean radar is the ground wave radar. The loss of radio waves is the largest for $j_b = 4$, because the radio wave path is affected

by the land, whose conductivity is much lower than that of seawater (Figure 1).

4. Results

4.1. Wave and Wind Fields

[26] Figure 3 shows time series of significant wave heights (H_s) and periods (T_s) at Ky (Figure 1), as well as hourly wind vectors ($\mathbf{U}_I = (U_I \cos \theta_I, U_I \sin \theta_I)$) at I (Figure 1) during the HF radar observation period. The significant wave height $H_s = 4.5$ m was the largest on 23 August 1995, and was associated with the passage of tropical cyclone (typhoon) Janis near the HF radar observation area [Hisaki and Naruke, 2003]. The maximum wind speed was 14.5 m/s during this period. The wave period was $T_s = 9$ s on 23 August 1995, which was not the longest period during the observation period. The perturbation theory of HF radio wave scattering from the sea surface to the second order (equations (1) and (2)) can be applied in the case of wave heights are small compared to the radio wavelength. For example, Lipa and Barrick [1982] showed that a significant wave height of H_s , which is smaller than $2/k_0$, can be applied to second-order perturbation theory, while wave height is generally underestimated when it is higher. This underestimation is predicted by Hisaki [1999]. The significant wave height $H_s = 4.5$ m exceeds the limit of perturbation theory. On the other hand, Wyatt [1999] showed that wave height is underestimated in high sea-states because the Doppler spectrum at higher Doppler frequencies is much higher than that predicted by the theory.

[27] The wave height $H_s = 3.5$ m was also large on August 30 1995, although the wind speed reached a maximum of only 7 m/s. The longest wave period, which was $T_s = 11$ s, occurred on 31 August 1995, with a wind speed of 4 m/s. These wave and wind conditions suggest that a swell associated with the passage of typhoon Kent was dominant during this period. Kent formed in the Philippine Sea, and intensified as it approached the Luzon Strait. It then continued on a west-northwest track and made landfall in China, just east of Hong Kong [Ero and Bassi, 1995]. Although the closest distance between typhoon Kent and the HF radar observation area was approximately 850 km, Kent was very severe and the HF radar observation area was affected by the swell. The minimum center pressure was 945 hPa and the maximum wind speed was 43 m/s when the center location was around 20°N, 120°E on 30 August 1995. The wind direction was almost northward, and waves were in fetch-unlimited conditions during the most of the HF radar observation period. The wind direction was southwestward on 21 August, but waves in the HF radar observation area were also in fetch-unlimited conditions (Figure 1). If we assume that the wind direction at I was similar to that in the HF radar observation area, the wind directions would have been eastward or southeastward, and the fetch-limited wave conditions would have been encountered on 8 and 9 September 1995.

[28] Figure 4 shows the time series of waveheights (H_j), periods (T_j) and wave directions (θ_j) at 26° N and 128° E predicted by the JMA [1996]. The general tendency of changing wave heights and periods is the same as that shown in Figure 3. The wave height is the largest on 23 August 1995, and the wave period is the longest on 30 August 1995.

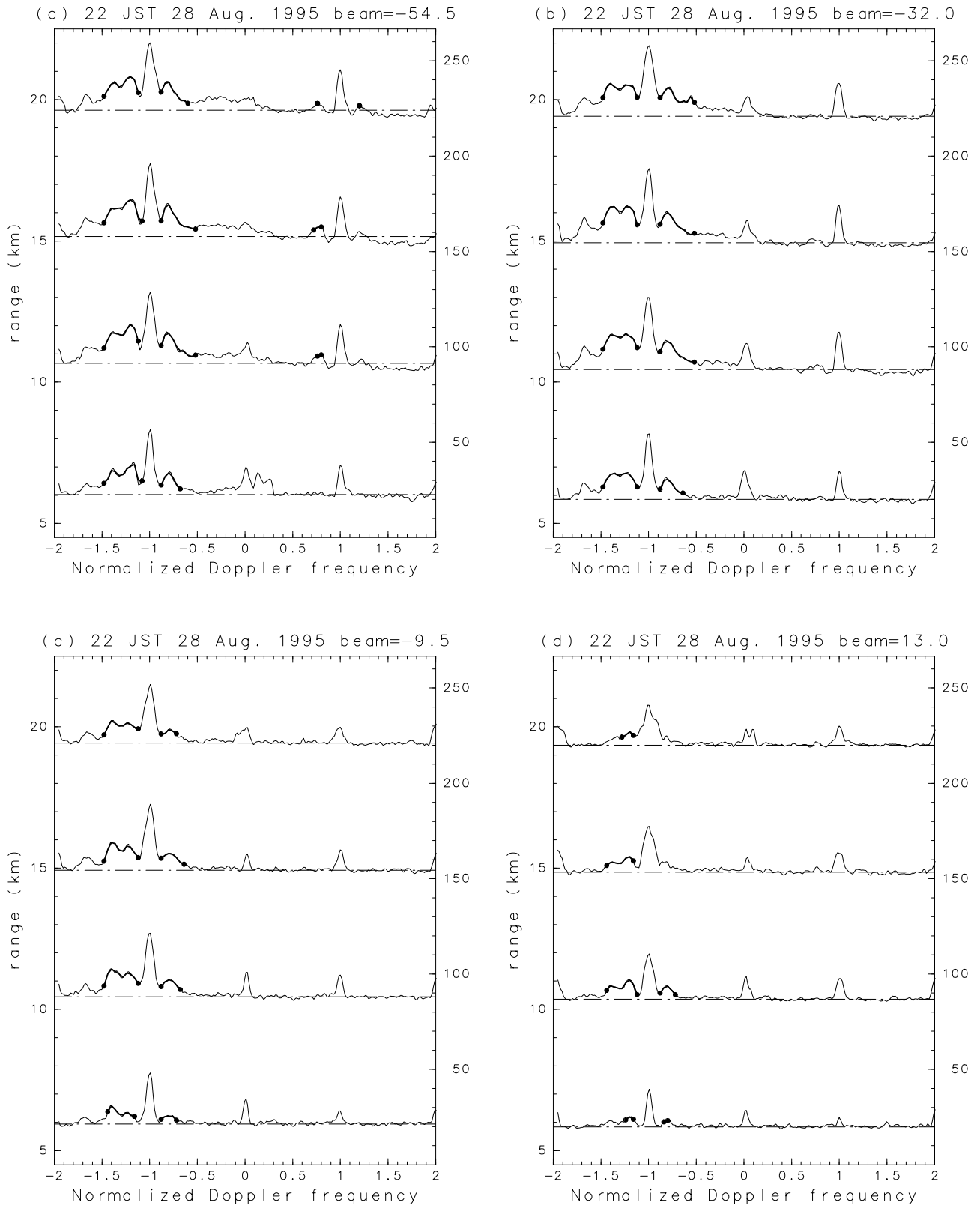


Figure 2. Examples of averaged Doppler spectra for beam numbers (a) $j_b = 1$, (b) $j_b = 2$, (c) $j_b = 3$, and (d) $j_b = 4$. Lines are shifted so that they do not overlap each other. Thick line, extracted second-order scattering region for estimating the wave spectrum; dash-dotted line, noise level. The left vertical axis indicates the distance of each Doppler spectrum from the radar. The right vertical axis indicates the relative signal intensity in decibels.

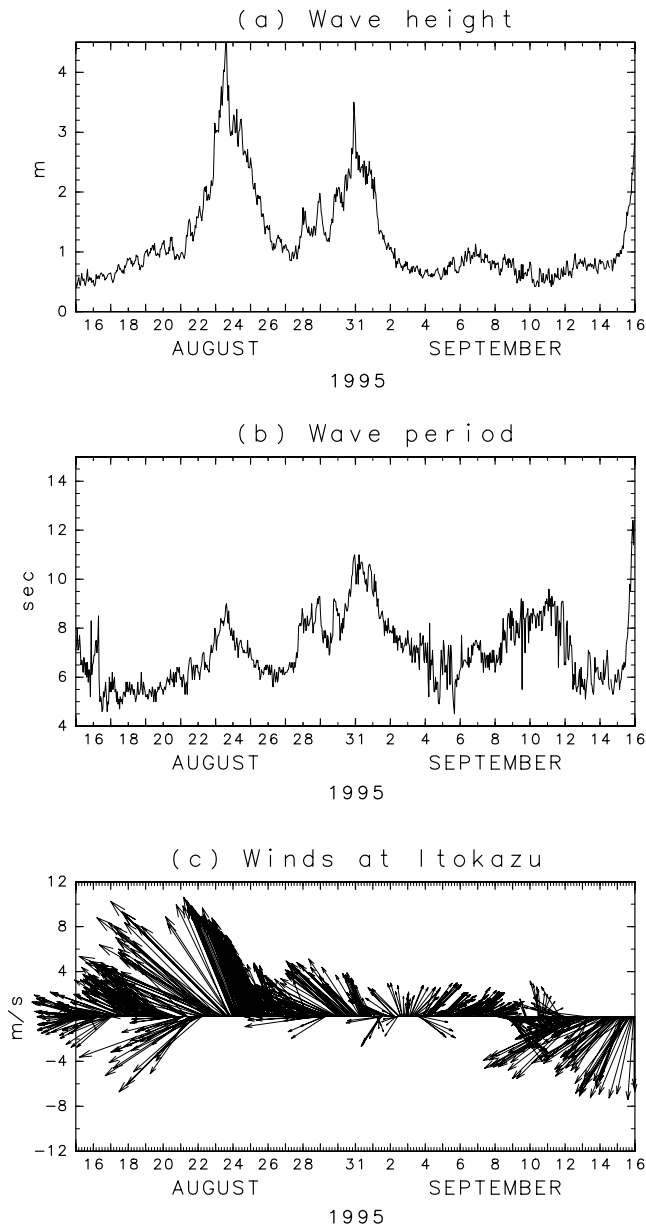


Figure 3. Time series of (a) significant wave heights (H_s) and (b) periods (T_s) at Ky (Figure 1). (c) Hourly wind vectors ($\mathbf{U}_I = (U_I \cos \theta_I, U_I \sin \theta_I)$) at I (Figure 1) during the HF radar observation period.

The wave direction on 30 and 31 August was northward, when swell was dominant.

4.2. Comparison of Wave Parameters

[29] The wave spectra at 2-hour intervals from 21 August to 10 September 1995 (252 time series) were estimated. The weights in equation (8) are $\lambda_{w1} = (\nu_1/\nu_2)^{1/2}$, $\lambda_{w2} = \lambda_{w3} = \lambda_{w5} = \lambda_{w6} = 1$, and $\lambda_{w4} = 10^2$. In the second step of the initial guess (see section 2.2), the weights are $\lambda_{w1} = (\nu_1/\nu_2)^{1/2}$, and $\lambda_{w5} = 0.1$ (hereafter referred to as case 1). The value of ν_1 in λ_{w1} is the degrees of freedom of the integrated first-order Doppler spectrum, and the value of ν_2 is the degrees of freedom of the second-order Doppler spectrum. The degrees of freedom at one Doppler spectral

point are 11 [Hisaki, 1999], and $\nu_2 = 11$. The degrees of freedom of the integrated first-order Doppler spectrum are approximately $1.3M_h \times 11$, where M_h is the number of spectral points greater than half of the maximum Bragg peak level within the Bragg echo region [Barrick, 1980]. A typical value of M_h is 5, and $\nu_1 = 72$. There are no good ways at present to determine the optimal values of weights λ_{wM} in equation (8). We compare the wave parameters for other pairs of λ_{wM} ($M = 1, \dots, 6$), and discuss the effect of variations.

[30] The wave parameters are compared with those at station Ky (Figure 1). Wave parameters are calculated from

$$E_n = E_n(\alpha) = \int_{\omega_{\min}}^{\omega_{\max}} \int_{-\pi}^{\pi} G(\omega, \theta) \alpha^n d\theta d\omega, \quad (9)$$

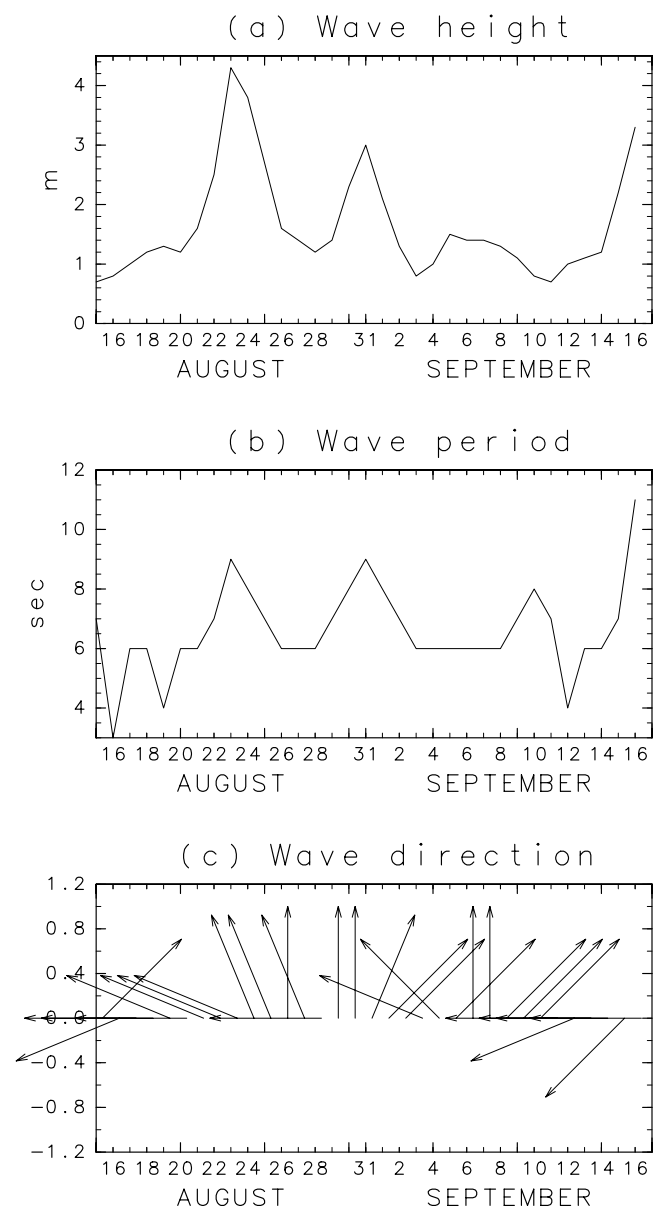


Figure 4. Time series of (a) wave heights H_j , (b) periods T_j and (c) wave directions ($\cos \theta_j, \sin \theta_j$) at 26°N and 128°E predicted by the JMA.

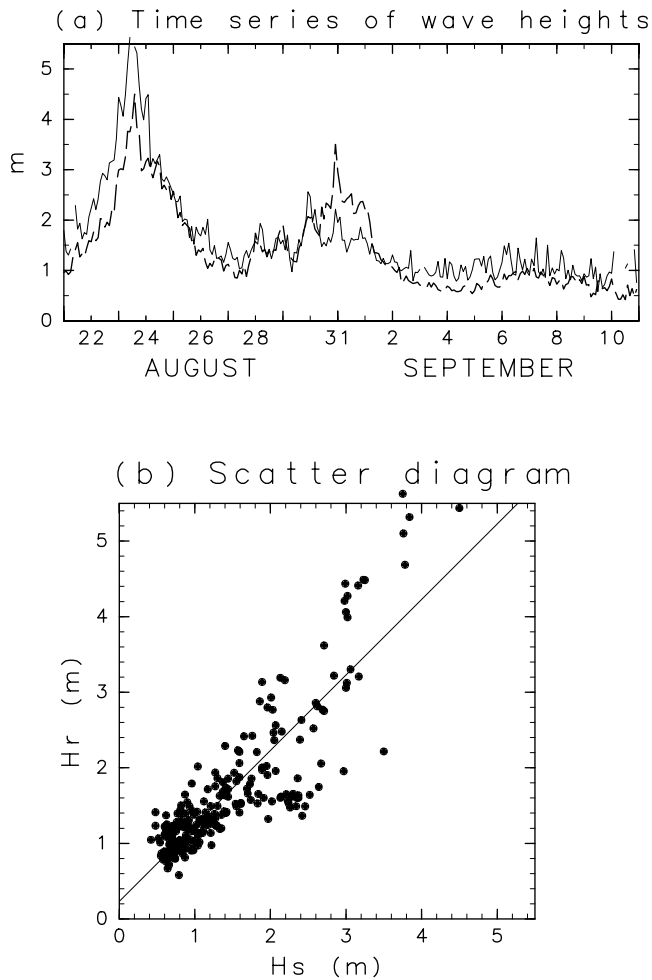


Figure 5. Comparison between JMA significant wave heights H_s and radar-estimated wave heights H_r at $(i_r, j_b) = (1, 3)$ for case 1. (a) Time series (solid line, H_r ; dashed line, H_s) and (b) scatter diagram.

where α is the parameter of waves such as ω . The radar-estimated wave height is calculated as $H_r = 4E_0^{1/2}$.

[31] Figure 5 shows the comparison between JMA-estimated wave heights (H_s) and radar-estimated wave heights (H_r) at $(i_r, j_b) = (1, 3)$. The nine radar-estimated wave heights showed abnormal values and excluded. The correlation coefficient between H_s and H_r was $R_c = 0.87$, and the RMS difference $\Delta_{rms}(H_s, H_r) = \langle (H_s - H_r)^2 \rangle^{1/2}$ was 0.52 m, where $\langle \dots \rangle$ denotes averaging. The slope and bias of the linear regression line (a and b for $H_r = aH_s + b$) are $a = 1.02$ and $b = 0.23$ m, respectively. The RMS difference from the linear regression line was $\Delta_{rms}(H_s, aH_s + b) = 0.47$ m, and the comparisons are summarized in Table 1. The radar-estimated wave heights (H_r) were larger than the JMA-estimated wave heights (H_s) during most of the observation period. However, JMA wave heights (H_s) were larger than radar-estimated wave heights (H_r) from 30 August to 1 September 1995, when swell was dominant. In general, the agreement between H_r and H_s is good.

[32] The JMA significant wave period (T_s) was estimated by the zero-up-cross method. While there is a definite relationship between significant wave heights and $E_n(\omega)$

(i.e., $H_s = 4E_0^{1/2}$), there are no definite relationships between T_s and $E_n(\omega)$. The moment period $T_m = 2\pi E_0^{1/2} E_2(\omega)^{-1/2}$ is compared with the JMA significant wave period (T_s). Figure 6 shows the comparison between JMA significant wave periods (T_s) and radar-estimated moment wave periods (T_m) at $(i_r, j_b) = (1, 3)$. The correlation coefficient between T_s and T_m was $R_c = 0.31$ (Table 1), and the correlation is small. However, the general tendency of change of wave periods T_m is similar to that of T_s . For example, both T_m and T_s were larger on 23 August and 1 September 1995. The large T_m on September 1 shows that it is possible to estimate the swell period from HF ocean radar. The correlation between T_s and T_m from 21 August to 1 September was $R_c = 0.57$. Nevertheless, there are no correlations between T_s and T_m on 2 September, when wave heights were small and wave periods were short. The mean value of T_s/T_m was 1.53, which is consistent with Goda [2000].

4.3. Comparison of Wind Parameters

[33] There are no observations of sea surface winds, however, we can assume that winds at Itokazu are correlated with sea surface winds in the HF ocean observation area, and thus the winds at Itokazu are correlated with radar-estimated winds. Even in the identical twin experiment, the accuracy of wind speeds is poorer than that of other wave parameters [Hisaki, 2005]. Because time and spatial scales for winds and waves are different, the relationship between wind speeds and the Doppler spectra is not straightforward. The accuracy of retrieved wind speeds is several times poorer than that of other wave parameters such as wave heights and wave periods under short-fetch conditions [Hisaki, 2005].

[34] Figure 7 shows the comparison between JMA wind speeds at Itokazu (U_I) and radar-estimated wind speeds (u_w) at $(i_r, j_b) = (2, 4)$. The radar-estimated wind speeds were correlated with JMA wind speeds at Itokazu. The correlation coefficient between U_I and u_w was $R_c = 0.75$, and the RMS difference from the linear regression line was 1.9 m/s (Table 1). The correlation coefficient from 30 August to 1 September, when swell was dominant, was $R_c = 0.70$, showing that it is possible to estimate wind speeds from HF radar Doppler spectra, although there remains room for improvement. In some cases, wind speeds are overestimated, which is due to the overestimation of spectral values at higher frequencies.

[35] The sea surface wind direction was estimated from the ratio of two first-order scatterings [e.g., Hisaki, 2002]. The short-wave directional distribution was expressed as $\cos^{2s}((\theta - \theta_w)/2)$, where s is the spreading parameters, and s and θ_w were estimated. Although wind directions are also unknowns in constraints (C1)–(C6) in section 2, the initial

Table 1. Comparison Between HF Ocean Radar-Derived Parameters and Japanese Meteorological Agency (JMA) Parameters

	$H_s - H_r$	$T_s - T_m$	$u_w - U_I$	$\theta_I - \theta_w$	$H_s - H_r$ (Case 2)
R_c	0.87	0.31	0.75	0.88	0.83
Δ_{rms}	0.52, m			49.6°	0.67, m
Regression line					
a	1.02	0.19	0.61	0.93	0.99
b	0.23, m	3.54, s	0.39, m/s	-14.7°	0.45, m
Δ_{rms}	0.47, m	0.71, s	1.92, m/s	44.1°	0.52, m

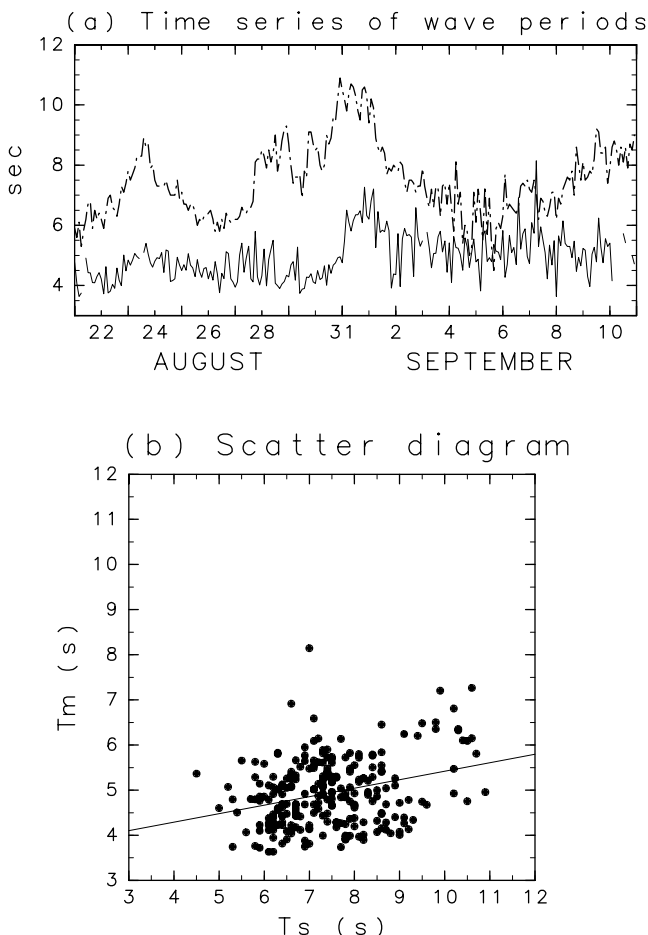


Figure 6. Comparison between the JMA significant wave period T_s and radar-estimated moment wave periods T_m at $(i_r, j_b) = (1, 3)$ for case 1. (a) Time series (solid line, T_m ; dashed line, T_s) and (b) scatter diagram.

guess of wind directions is determined from the ratio of two first-order scatterings. The parameters s and θ_w are estimated assuming that these parameters are not dependent on radial grids (i_r, j_b) in the initial guess. The estimated wind vectors are dependent on the initial guess.

[36] Figure 8 shows the comparison between JMA wind directions at Itokazu (θ_I) and radar-estimated wind speeds (θ_w) at $(i_r, j_b) = (2, 4)$. The correlation coefficient was $R_c = 0.88$ (Table 1), and it was found to be possible to estimate wind directions by HF ocean radar. However, the accuracy of estimations of wind direction was poorer than those of *Hisaki* [2002]. The RMS difference from the linear regression line is 31° in the work of *Hisaki* [2002], but 44° in the present case. Note that dual radars were used by *Hisaki* [2002], while a single radar was used in the present study. In the case of single radar, the solution of (s, θ_w) was not determined uniquely.

4.4. Sensitivity to Weights

[37] The estimated wave spectra are dependent on λ_{wM} ($M = 1, \dots, 6$). We calculated wave spectra for other pairs of λ_{wM} ($M = 1, \dots, 6$). The weights in equation (8) are $\lambda_{w1} = (72/11)^{1/2}$, $\lambda_{w2} = \lambda_{w3} = \lambda_{w6} = 1$, $\lambda_{w5} = 0.1$ and $\lambda_{w4} = 10^2$ (hereafter referred to as case 2). The weights in the second

step (see section 2.2) are the same as those in case 1. Only the parameter λ_{w5} in the third step is different from that in case 1.

[38] Figure 9 shows the comparison between JMA wave heights (H_s) and radar-estimated wave heights (H_r) at $(i_r, j_b) = (1, 3)$ for case 1. The correlation coefficient between JMA significant H_s and H_r was $R_c = 0.83$, and the RMS difference was $\Delta_{rms}(H_s, H_r) = 0.67$ m (Table 1). The radar-estimated wave heights for case 2 were larger than those for case 1, and the accuracy was poorer; however, there are 38 samples that satisfy $|H_r(\text{case 2}) - H_s| < |H_r(\text{case 1}) - H_s|$, which are shown in Figure 9. Specifically, the values of H_r for case 2 are closer to H_s than those for case 1 from 30 August to 1 September when swell was dominant. This result shows that the weight λ_{w5} should be smaller when swell is dominant. The value $\lambda_{w5} = 1$ tends to oversmooth for swell conditions, because the wave spectral peak associated with the swell is sharper than that of wind waves.

[39] Wave spectra for other pairs of λ_{wM} ($M = 1, \dots, 6$) are also calculated for: case 3, same weights as case 1 but for

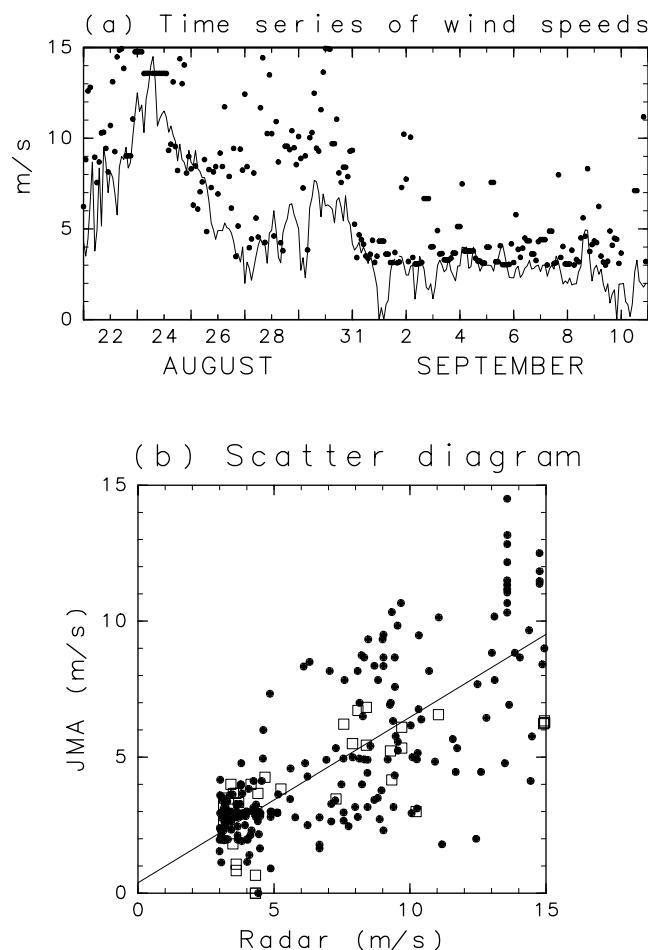


Figure 7. Comparison between radar-estimated wind speeds u_w at $(i_r, j_b) = (2, 4)$ and JMA wind speeds at Itokazu U_I for case 1. (a) Time series (solid line, U_I ; solid circle, u_w) and (b) scatter diagram (open rectangle: U_I and u_w from 0000 Japanese Standard Time (JST) to 2200 JST on 30 August 1995).

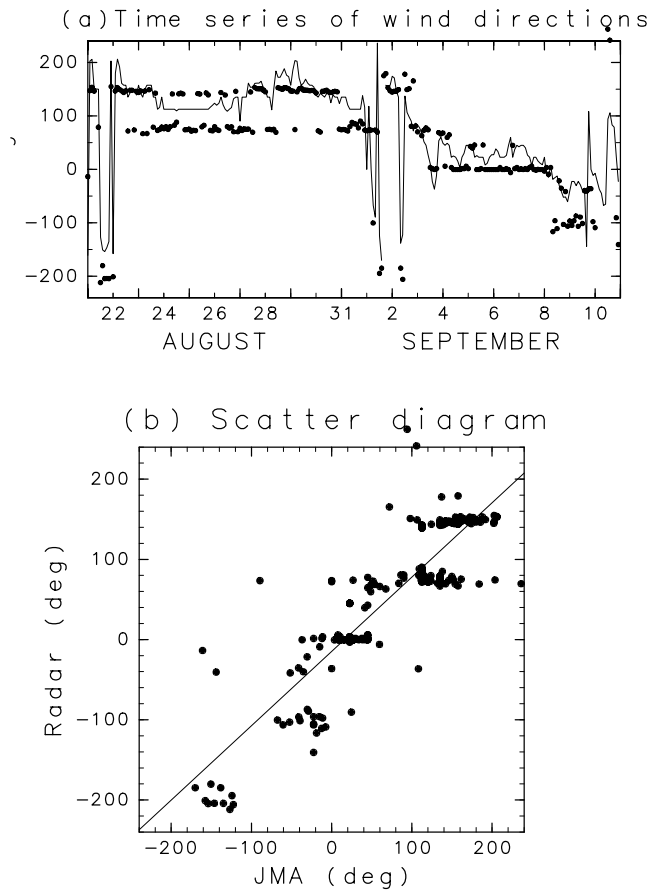


Figure 8. Comparison between JMA wind directions at Itokazu θ_j and radar-estimated wind directions θ_w at $(i_r, j_b) = (2, 4)$ for case 1. (a) Time series (solid line, θ_j ; solid circle, θ_w) and (b) scatter diagram.

$\lambda_{w5} = 10$; case 4, same weights as case 1 but for $\lambda_{w3} = \lambda_{w6} = 0.1$; case 5, same weights as case 1 but for $\lambda_{w3} = \lambda_{w6} = 10.0$; case 6, same weights as case 1 but for $\lambda_{w3} = 0.01$ in the second step (section 2.2); and case 7, same weights as case 1 but for $\lambda_{w3} = 1.0$ in the second step. Table 2 summarizes the comparison between radar-estimated wave heights at $(i_r, j_b) = (1, 3)$ and in situ observations. The effect of varying weights on wave estimation is not large. In case 3, the difference between radar-estimated wave heights and in situ observations is somewhat smaller than that in case 1. Because radar-estimated wave heights tend to be over-estimated except in swell conditions as in case 1, the agreement of wave heights is improved in case 3. On the other hand, there are no significant differences in wave estimation between case 1 and cases 4 or 5. We also investigated the effect of varying weights λ_{w4} and λ_{w6} on wave estimation, and found that the effect was small. The weight λ_{w3} (regularization constraints in frequency-direction grids) is the most important for wave estimation.

[40] The difference in wave estimation between cases 1 and 6 is also small, however, the accuracy of radar-estimated wave heights for case 7 is poorer than that for case 1. Because the number of iterations is limited, the estimated wave spectra are dependent on the initial guess. The initial wave spectra estimated in the second step

(section 2.2) are not dependent on the radial grid points. Therefore the initial wave spectra are not less sensitive to the noise in measured Doppler spectra than wave spectra estimated in the third step. The weight λ_{w3} (constraint C3) in the second step is expected to be smaller than that in the third step.

4.5. Examples of Observed Waves

[41] Figure 10 shows the mean wave heights during the HF radar observation period for case 1. The radar-estimated wave heights H_r , which are significantly different from H_s , are not used for the average. Most of the wave conditions were fetch-unlimited during the observation period, and the wave fields were almost homogeneous. The wave heights were larger in the eastern part of the HF radar observation area, where fetch is longer and wind speeds are larger because of its offshore location. Nevertheless, the difference between minimum and maximum mean wave heights was only approximately 0.15 m.

[42] Figure 11 shows the time series of radar-estimated mean wave direction θ_r at $(i_r, j_b) = (4, 3)$ for case 1, JMA wind directions at Itokazu (θ_j) and JMA wave directions θ_j (Figure 4c). The radar-estimated mean wave direction is $\theta_r =$

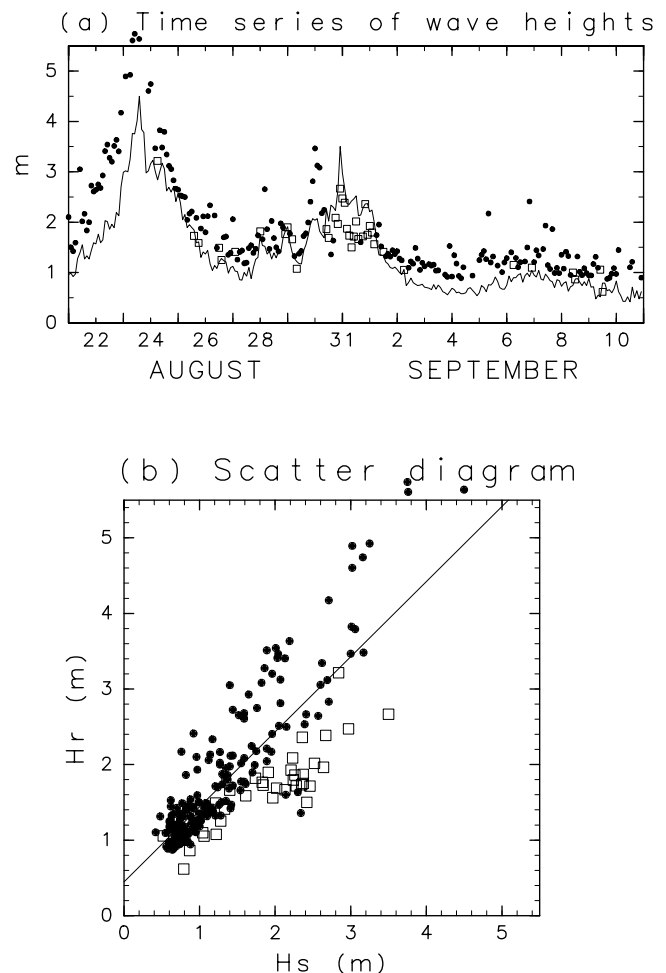


Figure 9. Same as Figure 5 but for case 2. Open rectangles show the radar-estimated wave heights for case 2 ($H_r(\text{case 2})$), when $|H_r(\text{case 2}) - H_s| < |H_r(\text{case 1}) - H_s|$.

Table 2. Comparison Between JMA Wave Heights for Various Parameters H_s and HF Ocean Radar-Derived Wave Heights H_r .

	Case 3	Case 4	Case 5	Case 6	Case 7
R_c	0.87	0.86	0.85	0.84	0.69
Δ_{rms}	0.45, m	0.52, m	0.53, m	0.56, m	0.74, m
Regression line					
a	0.91	0.98	0.98	0.99	0.78
b	0.25, m	0.26, m	0.27, m	0.28, m	0.79, m
Δ_{rms}	0.43, m	0.46, m	0.47, m	0.51, m	0.53, m

$E_1(\theta)E_0^{-1}$, and the center of the numerical integration range with respect to the direction θ for calculating $E_1(\theta)$ is the peak direction. If the directional distribution is symmetrical with respect to the peak direction, θ_r is equal to the peak direction.

[43] Most of the radar-estimated wave directions are close to either JMA wind directions (θ_j) or JMA wave directions (θ_w). However, there are some cases in which radar-estimated wave directions are significantly different from both JMA wind directions and JMA wave directions, indicating that left-right ambiguity was not removed in these cases. Left-right ambiguity with respect to the radar radial was removed from constraints (C3) (equation (4): energy balance equation) and (C6) (equation (7): regularization constraints in spatial radial grids) in section 2. For a

given wave height and wave directional distribution, the second-order Doppler spectrum is the smallest where the dominant wave propagates perpendicular to the beam direction. The sensitivity of the Doppler spectrum shape to the dominant wave direction is the smallest in the perpendicular case. Therefore the removal of ambiguity is affected by the noise, especially when the wave direction is perpendicular to the boresight direction: -110° or 70° ($\psi_a = -20.75^\circ$).

[44] The radar-estimated wave directions were closer to the JMA wave directions than to the JMA wind directions for 30 and 31 August when swell was dominant. On the other hand, the radar-estimated wave directions were closer to the JMA wind directions than to the JMA wave directions on 3 and 4 September.

[45] Figure 12 shows examples of radar-estimated wave spectra at $(i_r, j_b) = (4, 1)$. Figures 12a and 12c are the frequency spectra $\Psi(f)$, and Figures 12b and 12d are the normalized directional distributions $D(f, \theta) = 2\pi G(\omega, \theta)/\Psi(f)$, where $f = \omega/(2\pi)$ is the wave frequency. The integral of the normalized directional distributions $D(f, \theta)$ with respect to the direction θ is 1. Figures 12a and 12b are radar-estimated wave spectra for case 1 at 10 Japanese Standard Time (JST) on 24 August when the wave height was large due to the typhoon (Figures 3 and 5a). The JMA significant wave height is $H_s = 3.17$ m, and the radar-estimated wave height is $H_r = 3.3$ m; the peak wave

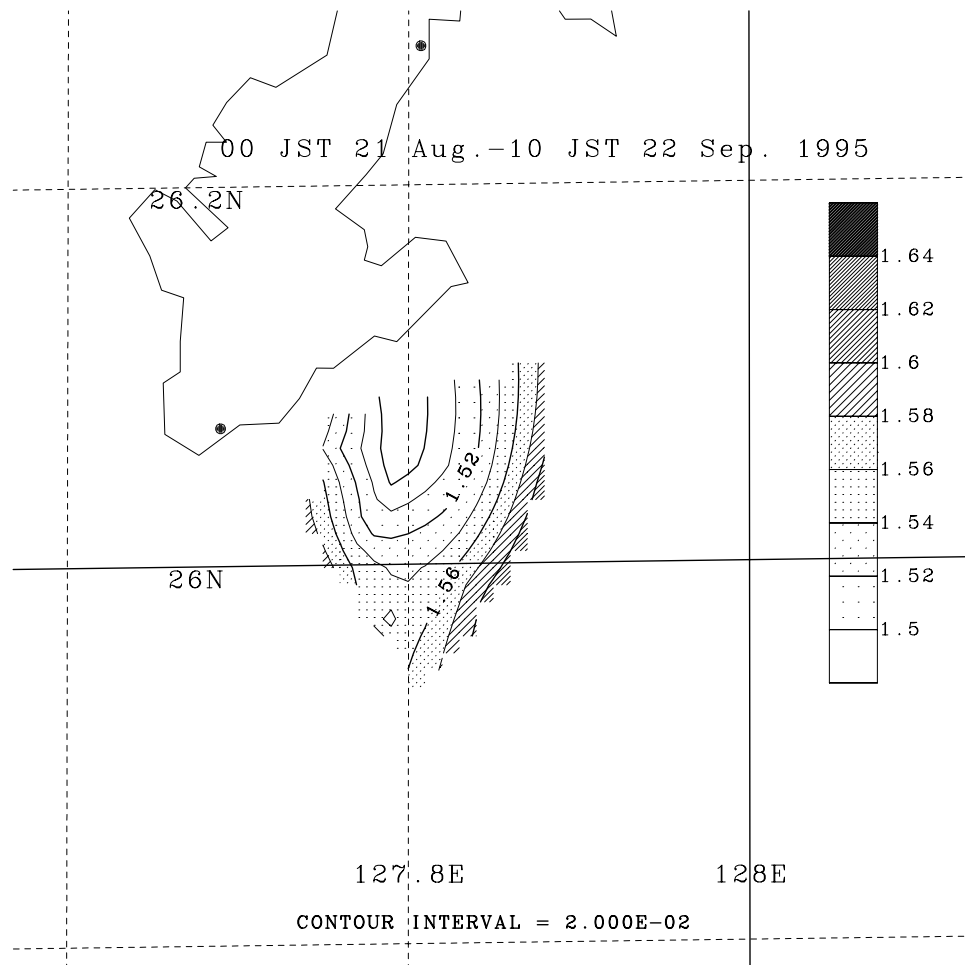


Figure 10. Mean wave heights during the HF radar observation period for case 1. Unit is meters.

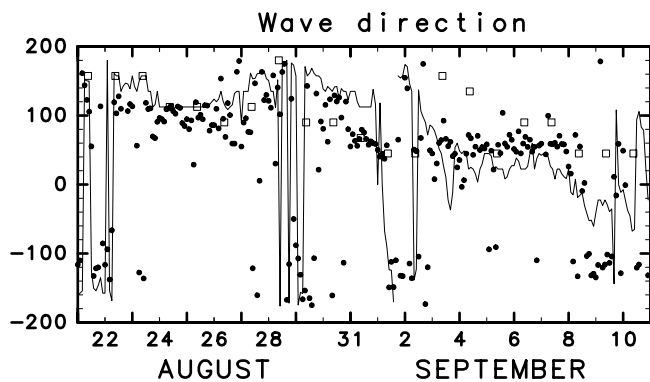


Figure 11. Time series of radar-estimated mean wave direction θ_r at $(i_r, j_b) = (4, 3)$ for case 1 (solid circle), JMA wind directions at Itokazu θ_I (solid line) and JMA wave directions θ_J (open rectangle).

frequency is 0.115 Hz. Figures 12c and 12d are radar-estimated wave spectra for case 2 at 2 JST on 31 August when swell was dominant. The JMA significant wave height is $H_s = 2.67$ m, and the radar-estimated wave height is $H_r = 2.31$ m; the peak wave frequency is 0.1 Hz. Although the wave height in Figure 12c is smaller than that in Figure 12a, the peak wave frequency in Figure 12c is lower than that in Figure 12a. In addition, the directional distribution in Figure 12d is narrower than that in Figure 12b near the peak frequency. These facts indicate that the spectral peak in Figure 12c shows swell, that is, the present method is capable of identifying swell.

5. Discussion and Conclusion

[46] The method proposed by Hisaki [2005] to estimate ocean wave spectra from HF ocean radar was applied to observed Doppler spectra. The method is based on the integral equation, which relates first- and second-order Doppler spectra to the wave spectrum, the energy balance equation and regularization constraints. The integral equation which relates the second-order Doppler spectrum to the wave spectrum is discretized in the nonlinear form. Thus the present method can dynamically extrapolate wave spectra at positions where the SN ratio of Doppler spectra is not good. During the HF radar observation period, the wave field was affected by a typhoon. As a result, there was a period when swell was dominant. Wave parameters estimated by HF ocean radar were compared with in situ observations, and the agreement of radar-estimated wave heights H_r and JMA significant wave heights H_s was found to be good. Nevertheless, there were some cases in which radar-estimated wave heights were found to be overestimated. Doppler spectra are significantly affected by noise, causing wave heights to be overestimated.

[47] The correlation between radar-estimated moment periods T_m and JMA significant wave periods T_s estimated by the zero-up-cross method was not good, probably because there are no definite relationships between moment period and significant wave period. Nevertheless, the mean value of T_s/T_m is consistent with that found in previous study [Goda, 2000], and a correlation was identified between T_s and T_m from 21 August to

1 September, when the wave heights and periods changed significantly.

[48] There was found to be a correlation between radar-estimated wind speeds and wind speeds at the station near the HF radar observation area, even in swell conditions. However, there remain cases in which wind speeds were overestimated due to the overestimation of spectral values at higher frequencies, because the initial guess of wind speeds is determined from spectral values at higher frequencies. The method using spectral values at higher frequencies is promising for wind speed estimation from HF ocean radar because it can be applied in both wind wave and swell conditions. The proposed method by Dexter and Teodoridis [1982], which uses the relationship between wind speed and radar-estimated wave parameters, can be applied only in wind wave conditions. It is possible to estimate spectral values at higher frequencies only by nonlinear inversion, because linear inversion assumes that spectra form at higher frequencies, and spectral values at higher frequencies are not estimated. In the linearization of the integral equation relating the second-order radar cross section to the ocean wave directional, the short-wave directional spectrum is replaced with the spectral form inferred from the first-order scattering [e.g., Lipa and Barrick, 1986].

[49] It is possible to estimate wind direction from a single radar, however, accuracy is poorer than that of estimations made using dual radar data. Noise affects the estimation of wind direction with a single radar more seriously than with dual radar. The wind directions are determined primarily in the first step (section 2.2), and are obtained by estimating (s, θ_w) for the $\cos^{2s}((\theta - \theta_w)/2)$ directional distribution from first-order Doppler spectrum ratios [e.g., Hisaki, 2002]. In general, noise is not a problem in determining wind direction, since it is obtained from first-order peaks that are well above the noise. A possible explanation of the discrepancy is that the parameters (s, θ_w) are not determined uniquely for observed first-order ratios. First-order Doppler spectrum ratios are not sensitive to noise, but the solution (s, θ_w) is sensitive to noise for the observed first-order ratios.

[50] The radar-estimated wave directions in the present study are consistent with JMA-estimated wave directions and wind directions. During the swell period, radar-estimated wave directions were closer to JMA wave directions than to JMA wind directions; however, there are cases in which left-right ambiguity cannot be removed. The removal is affected by the noise, especially if the wave is almost perpendicular to the beam direction.

[51] The initial guess is important for estimating wave spectra and winds, not only because the convergence speed depends on it but also because the iteration does not seek the global minimum of $U(\mathbf{x})$ but rather the local minimum of $U(\mathbf{x})$. If the initial values of wave spectra in the first step are arbitrary, the algorithm did not converge to the solution [Hisaki, 2005]. The present method to obtain initial guess is valid from the result in section 4, but it is necessary to develop the method of seeking the global minimum of $U(\mathbf{x})$.

[52] The optimal values of weights λ_{wM} ($M = 1, \dots, 6$) are dependent on wave conditions. For example, the weights for regularization constraints in the wave frequency-direction

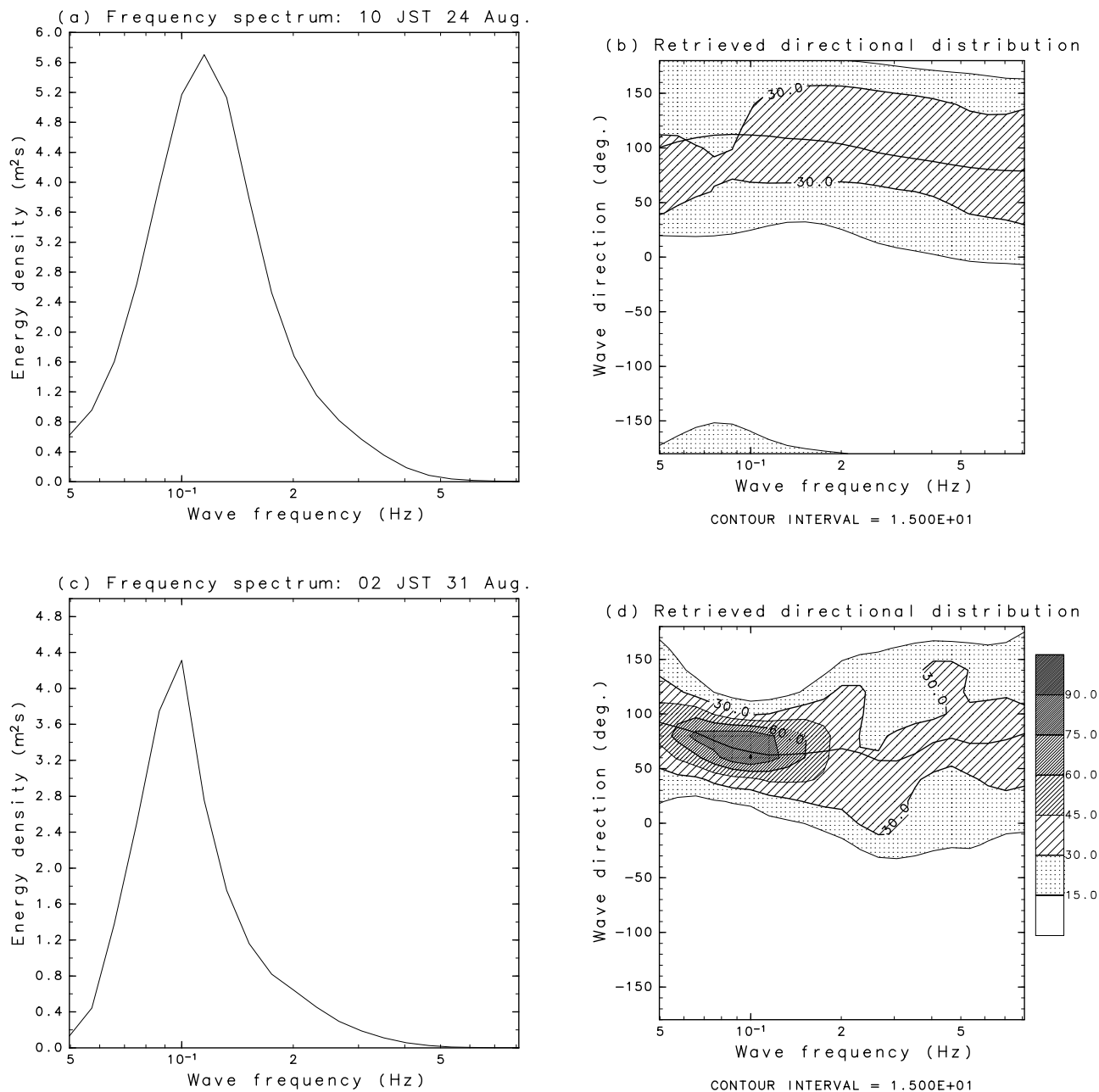


Figure 12. (a) Radar-estimated frequency spectra $\Psi(f)$ for case 1 at 1000 JST on 24 August 1995, (b) normalized directional distributions $D(f, \theta) = 2\pi G(\omega, \theta)/\Psi(f)$ (%) for case 1 at 1000 JST on 24 August 1995, (c) same as Figure 12a but for case 2 at 0200 JST on 31 August 1995, and (d) same as Figure 12b but for case 2 at 0200 JST on 31 August 1995. The lines in Figure 12b and 12d show mean directions as a function of wave frequency.

plane area smaller in swell-dominant conditions. The radar-estimated wave directional spectrum during the swell in the present observation period shows a lower peak frequency and narrow directional distribution.

[53] The final goal of the present study was to develop a method of estimating ocean wave spectra from HF ocean radar robust to noise. Therefore we must develop an algorithm to extract first- and second-order scattering, even though the Doppler spectrum is significantly contaminated by the noise. Furthermore, a method of easily determining the best values of weights λ_{wM} ($M = 1, \dots, 6$) also remains to

be developed, together with an algorithm to control data quality.

[54] **Acknowledgments.** The author would like to thank the staff of Okinawa Radio Observatory, Communications Research Laboratory (Okinawa Subtropical Environment Remote-Sensing Center, National Institute of Information and Communications Technology), for providing the Doppler spectrum data, and the Japan Meteorological Agency for providing the meteorological data. The insightful comments of the anonymous reviewers contributed greatly to the improvement of the manuscript. This study was supported financially by a Grant-in-Aid for Scientific Research (C-2) from the Ministry of Education, Culture, Sports, Science

and Technology of Japan (16540403). The GFD-DENNOU Library (<http://dennou.gaia.h.kyoto-u.ac.jp/arch/dcl/>) was used for drawing the figures.

References

- Barrick, D. E. (1971), Dependence of second-order Doppler sidebands in HF sea echo upon sea state, paper presented at International Symposium, IEEE Antennas and Propag. Soc., Los Angeles, Calif.
- Barrick, D. E. (1980), Accuracy of parameter extraction from sample-averaged sea-echo Doppler spectra, *IEEE Trans. Antennas Propag.*, *AP-28*, 1–11.
- Barrick, D. E., M. W. Evans, and B. L. Weber (1977), Ocean surface currents mapped by radar, *Science*, *198*, 138–144.
- Dexter, P. E., and S. Teodoridis (1982), Surface wind speed extraction from HF skywave radar Doppler spectra, *Radio Sci.*, *17*, 643–650.
- Etro, J. F., and J. P. Bassi (1995), *1995 Annual Tropical Cyclone Report*, 289 pp., U.S. Nav. Pac. Meteorol. and Oceanogr. Cent. West, Joint Typhoon Warning Cent., Guam.
- Goda, Y. (2000), Random seas and design of maritime structures, in *Development of Wind Wave Spectra*, *Adv. Ser. Ocean Eng.*, 2nd ed., vol. 15, 464 pp., World Sci., Hackensack, N. J.
- Hashimoto, N., and M. Tokuda (1999), A Bayesian approach for estimation of directional wave spectra with HF radar, *Coastal Eng. J.*, *41*, 137–149.
- Hashimoto, N., L. R. Wyatt, and S. Kojima (2003), Verification of a Bayesian method for estimating directional spectra from HF radar surface backscatter, *Coastal Eng. J.*, *45*, 255–274.
- Hisaki, Y. (1996), Nonlinear inversion of the integral equation to estimate ocean wave spectra from HF radar, *Radio Sci.*, *31*, 25–39.
- Hisaki, Y. (1999), Correction of amplitudes of Bragg lines in the sea echo Doppler spectrum of an ocean radar, *J. Atmos. Oceanic Technol.*, *16*, 1416–1433.
- Hisaki, Y. (2002), Short-wave directional properties in the vicinity of atmospheric and oceanic fronts, *J. Geophys. Res.*, *107*(C11), 3188, doi:10.1029/2001JC000912.
- Hisaki, Y. (2004), Short-wave directional distribution for first-order Bragg echoes of the HF ocean radars, *J. Atmos. Oceanic Technol.*, *21*, 105–121.
- Hisaki, Y. (2005), Ocean wave directional spectra estimation from an HF ocean radar with a single antenna array: Methodology, *J. Atmos. Oceanic Technol.*, in press.
- Hisaki, Y., and T. Naruke (2003), Horizontal variability of near-inertial oscillations associated with the passage of a typhoon, *J. Geophys. Res.*, *108*(C12), 3382, doi:10.1029/2002JC001683.
- Hisaki, Y., and M. Tokuda (2001), VHF and HF sea-echo Doppler spectrum for a finite illuminated area, *Radio Sci.*, *36*, 425–440.
- Hisaki, Y., W. Fujiie, T. Tokeshi, K. Sato, and S. Fujii (2001), Surface current variability east of Okinawa Island obtained from remotely sensed and in situ observational data, *J. Geophys. Res.*, *106*, 31,057–31,073.
- Howell, R., and J. Walsh (1993), Measurement of ocean wave spectra using narrow beam HF radar, *IEEE J. Oceanic Eng.*, *18*, 296–305.
- Japan Meteorological Agency (1996), Ocean wave chart 1995, report, 243 pp., Jpn. Meteorol. Agency, Tokyo.
- Lipa, B. J., and D. E. Barrick (1982), CODAR measurements of ocean surface parameters at ARSLOE—Preliminary results, paper presented at Oceans 82 Conference, Inst. of Electr. and Electron. Eng., New York.
- Lipa, B. J., and D. E. Barrick (1986), Extraction of sea state from HF radar sea echo: Mathematical theory and modeling, *Radio Sci.*, *21*, 81–100.
- Prandle, D., and D. K. Ryder (1985), Measurement of surface currents in Liverpool Bay by high frequency radar, *Nature*, *315*, 128–131.
- Takeoka, H., Y. Tanaka, Y. Ohno, Y. Hisaki, A. Nadai, and H. Kuroiwa (1995), Observation of the Kyucho in the Bungo Channel by HF radar, *J. Oceanogr.*, *51*, 699–711.
- Uji, T. (1984), A coupled discrete wave model MRI-II, *J. Oceanogr. Soc. Jpn.*, *40*, 303–313.
- WAMDI group (1988), The WAM model—A third generation ocean wave prediction model, *J. Phys. Oceanogr.*, *18*, 1775–1810.
- Wyatt, L. R. (1990), A relaxation method for integral inversion applied to HF radar measurement of the ocean wave directional spectra, *Int. J. Remote Sens.*, *11*, 1481–1494.
- Wyatt, L. R. (1999), Evaluation of high frequency radar wave measurement, *Coastal Eng.*, *37*, 259–282.
- Wyatt, L. R. (2002), An evaluation of wave parameters measured using a single HF radar system, *Can. J. Remote Sens.*, *28*, 205–218.

Y. Hisaki, Department of Physics and Earth Sciences, Faculty of Science, University of the Ryukyus, 1 Aza-Senbaru, Nishihara-cho, Nakagami-gun, Okinawa 903-0213, Japan. (hisaki@sci.u-ryukyu.ac.jp)